Chapter 4

Spectroscopic mapping of the stellar and dark halo of the early-type galaxy NGC 2549

We obtain the stellar line-of-sight velocity distribution and absorption line strengths in the early-type edge-on galaxy NGC 2549 with the integral-field spectrograph PPAK. Combining four observed fields, we obtain a map out to more than four effective radii, probing the faint outskirts of this galaxy.

We find that NGC 2549 continues to rotate in a disc-like structure out to the edge of our observed field. From the kinematics and dynamical modeling, we infer that a second disc-like component is present, embedded in a larger, thicker disc. We use stellar population models to obtain age, metallicity and stellar mass-to-light ratios, based on stellar absorption line strength measurements. For the first time we map all these three quantities over the total field-of-view, finding again evidence for a flattened, young metal-rich component in the central part of the galaxy. The stellar halo population has an age of $\sim$9 Gyr, and we observe a change in metallicity from [Z/H] = 0.2 to [Z/H] = -0.4 from the centre to the edge of the observed field.

Schwarzschild dynamical models indicate that NGC 2549 is surrounded by a dark matter halo. Within one R_e, at least 16 per cent of the total mass is dark. At 5 R_e, this fraction has increased to 63 per cent. Applying anisotropic Jeans modeling to the observed kinematics supports this conclusion. We note however that these fractions are lower limits. If we incorporate in our models the stellar mass-to-light ratio resulting from stellar population modeling, the dark matter fraction within 1 R_e is already 65 per cent, and increases to 95 per cent at 5 R_e.

Anne-Marie Weijmans, Joris Gerssen, Michele Cappellari, P. Tim de Zeeuw,
Jesús Falcón-Barroso, Harald Kuntschner & Remco C.E. van den Bosch
To be submitted to *Monthly Notices of the Royal Astronomical Society*

4.1 Introduction

The outskirts of galaxies are still mostly unexplored territory, yet they harbour important clues for the formation history of these objects. Outside a few half-light or effective radii (R_e), dark matter starts to dominate over the luminous content of the galaxy. Dark haloes formed the gravitational potential wells in which gas could cool and form stars (e.g. Springel et al. 2005). Their mass and shape, together with stellar populations and their change in e.g. age and metallicity over large radii, constrain the starformation and assembly history of galaxies (e.g. Hopkins et al. 2009b). In addition, outer stellar substructures, such as tails, are tracers of past merger events (e.g. Schweizer 1986), and numerical simulations needed to interpret these features are generally more robust and less resolution dependent for large scale outer structures, than for central, smaller components.

It was recently shown by Weijmans et al. (2009a) that using integral-field units (IFUs) as photon collectors, it is possible to observe the stellar light in the faint outskirts of galaxies. The authors used the SAURON IFU (Bacon et al. 2001) to obtain stellar velocity profiles and absorption line strengths out to 3-4 R_e in two early-type galaxies. Because of the large collecting area of the IFU compared to traditional long-slit spectrography, and the relatively high throughput, the line-of-sight velocity dispersion (LOSVD) could be measured up to the fourth Gauss-Hermite moment h_4. This allowed breaking the mass-anisotropy degeneracy by means of constructing mass models. These models showed that dark matter haloes surround their observed galaxies, which out to 4 R_e make up 30 - 50 per cent of the total mass. In addition, they found that the line strength gradients observed in the central R_e of the galaxy (e.g. Kuntschner et al. 2006), continue out to at least 4 R_e. The same behaviour was seen for the well-studied Mg b-$V_{\rm esc}$ relation (e.g. Davies, Sadler & Peletier 1993; Scott et al. 2009). The stellar halo population was found to be old and metal-poor.

Because Weijmans et al. (2009a) could only sample the major axis of their targets, they did not construct fully general mass models, but assumed spherical dark haloes and maximal spheroids[1]. To allow modeling of more general halo profiles, more spatial coverage would be needed, while to relax the assumption of a maximal spheroid, a better handle of the stellar mass-to-light ratio (M_*/L) is required. We therefore turned to the PPAK integral-field unit (Kelz et al. 2006), which has a three times larger field-of-view and a longer wavelength coverage than SAURON. This last property allows for the measurement of more line

[1]Comparable to the maximal disc model that is often invoked for spiral galaxies, adopting the maximal M_*/L allowed by the data.

Morphological Type	S0
M_B (mag)	-19.44
Effective $B-V$ (mag)	0.95
Photometric PA ($^\circ$)	1
Distance modulus (mag)	30.45
Distance (Mpc)	12.3
Distance scale (pc arcsec^{-1})	60
Effective radius (arcsec)	20
Systemic velocity (km/s)	1070

Table 4.1 — Properties of NGC 2549. Magnitude and colour are taken from the Lyon/Meudon Extra galactic Database (LEDA). The distance modulus was derived from surface brightness fluctuation measurements by Tonry et al. (2001). Note that 0.06 mag is subtracted to adjust to the Cepheid zeropoint of Freedman et al. (2001); see Mei et al. (2005), section 3.3, for a discussion. The effective radius and position angle are taken from Cappellari et al. (2007).

strength indices, needed for an accurate determination of M_*/L as a function of radius. Although the spaxel size of PPAK is larger than that of SAURON (2.7 arcsec versus 0.94 arcsec), this loss in spatial resolution is not important when observing the outer parts of galaxies, where binning of spaxels is needed to obtain sufficient signal-to-noise (S/N) to measure kinematics and line strengths. For these faint observations it even helps to have large apertures, as the readnoise per collecting area is smaller.

We chose to observe the early-type field galaxy NGC 2549 out to 5 R_e with the PPAK IFU, to obtain the properties of its halo and stellar halo population. This isolated galaxy shows no signs of interactions and has an edge-on orientation, which simplifies mass modeling. NGC 2549 was also observed out to ~ 1 R_e as part of the SAURON survey (de Zeeuw et al. 2002), so that in the central part of our mass models, the PPAK data can be replaced by the higher resolution SAURON data. SAURON maps of the stellar kinematics, ionised gas, as well as line strengths were presented by Emsellem et al. (2004), Sarzi et al. (2006) and Kuntschner et al. (2006), respectively. Based on its stellar kinematic maps, NGC 2549 was classified as a fast rotator (Emsellem et al. 2007). Recently, Krajnović et al. (2009) modeled this galaxy combining SAURON and K-band NIFS integral-field kinematics, to measure the mass of the supermassive black hole residing in the centre of NGC 2549. This galaxy was not detected in atomic gas ($M_{\rm HI} < 2.0 \times 10^6 M_\odot$, Morganti et al. 2006) and kinematics of globular clusters or planetary nebulae have not been observed. This makes our observations of the

Field-of-view (arcsec × arcsec)	74 × 64
Fiber diameter (arcsec)	2.7
Number of science fibers	331
Number of sky fibers	36
Number of calibration fibers	15
Filling factor (per cent)	60

Table 4.2 — Properties of the PMASS PPAK spectrograph at the 3.5-m telescope at Calar Alto (see also Kelz et al. 2006).

stellar kinematics at large radii even more crucial, as no other tracer is available to constrain the dark halo. Some basic properties of NGC 2549 are summarized in Table 4.1.

We present our observations and datareduction in section 4.2. In section 4.3 we describe the extraction of the stellar and ionised gas kinematics, as well as the line strength measurements. Section 4.4 is devoted to interpretation of the line strength gradients and modeling of the stellar halo population. In section 4.5 we construct mass models of NGC 2549 and determine the properties of its dark halo. Finally, in section 4.6 we summarize and discuss our results.

4.2 Observations and data reduction

We observed the early-type galaxy NGC 2549 with the wide integral-field unit PPAK at the 3.5-m telescope at Calar Alto (Kelz et al. 2006, see also Table 4.2) in service mode. We used the V600 grating with a rotation of +144.4 degrees, so that it was centred on the Mg *b* absorption feature around 5200 Å. The hexagonal field-of-view (FoV) of PPAK was centred at 1.0 and at 3.2 R_e on the major axis of the galaxy, on opposite sides of the nucleus (see Figure 4.1). The FoV however has dimensions of 74 arcsec × 64 arcsec, and therefore the outer observations reach out to 5 R_e, probing the presumably dark matter dominated outskirts of the galaxy.

The observations were split in 1800 second individual exposures. Each exposure was bracketed by a calibration arc (HeHg + ThAr) and a trace continuum exposure (cont+cont). In addition we took a total of 28 blank sky exposures of 900 seconds, before or after each galaxy exposure[2]. These sky fields were used for sky subtraction, which is a critical aspect in our analysis: because we observe at

[2]In practice, this resulted in in an observing sequence of sky - galaxy -galaxy -sky etc., such that each galaxy exposure borders at least one sky exposure.

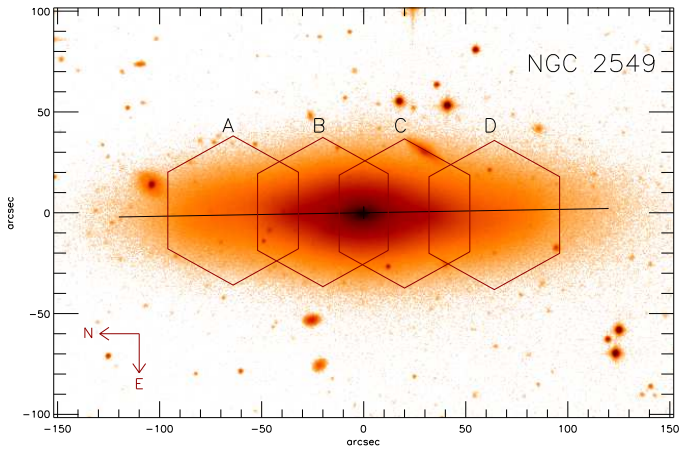

Figure 4.1 — Positions of our observed fields in NGC 2549 (red hexagonals), placed on the major axis of the galaxy (black line). The underlying V-band image was obtained with the 1.3-m McGraw-Hill Telescope at MDM Observatory.

very low surface brightness, our spectra are skydominated (see also Figure 4.2). PPAKs skyfibers are placed around the main fields at a distance of 1.2 arcmin from the central fiber and consequently they still observe faint galaxy light, and therefore do not provide an accurate enough sky subtraction for our observations. Also, the skyfields can be combined in a so-called superflat, to allow accurate flatfielding. A summary of our observations can be found in Table 4.3.

The data were reduced in IDL using the reduction package P3D (Sandin et al. 2009). This package performs the following steps. It creates and subtracts a master bias frame. It traces the location of each spectrum on the detector using the trace continuum exposures. The spectra in all science exposures are extracted by collapsing cross-dispersion profiles, centred on each trace position, to 1D spectra. As the spectra are fairly well separated on the detector (Kelz et al. 2006), the level of cross-talk between adjacent spectra is a few percent only. Hence we make no attempt to correct for cross-talk and simply apply a tophat weighting scheme when collapsing the spectra to 1D. Stacking of spectra to increase the S/N level in our subsequent analysis renders painstaking cross-talk correction unnecessary.

The continuum trace exposures and arclamp exposure are extracted similarly to the science exposures. The summed fluxes along each extracted trace spectrum are used to make a correction for the relative fiber-to-fiber throughput. In the extracted arclamp spectra the measured centroids of seven or eight He and Hg lines are fitted with a low order polynomial as a function of intrinsic wavelength

Field	R/R_e	T_{exp} (hr)	μ_V (mag/arcsec^2)
A	3.2	5.5	22.8
B	1.0	4.0	20.2
C	1.0	3.5	20.2
D	3.2	4.0	22.8

Table 4.3 — Properties of our observed fields in NGC 2549 (see Figure 4.1). The surface brightness μ_V in the centre of the pointing is calculated from the MDM images, and can be compared to the sky surface brightness, which at Calar Alto in V-band is about 22.0 mag/arcsec^2 in optimal conditions (Sánchez et al. 2007).

to derive the dispersion solution. All science spectra are rebinned onto the same wavelength scale using their individual, best-fit dispersion solutions.

We correct the different sky levels between exposures by normalising them using a 'superflat' field. The superflat is created by first median combining our 27 blank sky exposures into a single frame. A median sky spectrum is generated from the combined frame and smoothed by fitting it with a 4th order polynomial. The combined frame is divided by the smoothed sky spectrum to create the superflat.

After superflat fielding, the datacubes were imported in the XSAURON datareduction package, that was developed for the SAURON project (Bacon et al. 2001). We used this software to remove cosmic rays and to flux calibrate the spectra. For this last step, we used nightly observed spectra of the standard fluxstar G191-B2B. The spectra of the individual cubes were then resampled and interpolated on a rectangular grid and merged in a final datacube. We set the spatial resolution to 3 arcsec, which roughly corresponds to the distance between fiber centra. During the datareduction, the sky was not subtracted from the galaxy spectra, but was removed in a later stage, when extracting the stellar kinematics (see Section 4.3.1).

4.3 Extraction of kinematics and line strengths

To study the dark and stellar content of the halo of NGC 2549, we need to extract the stellar kinematics and line strengths from the spectra. To ensure that we have sufficient signal in each spectrum to reliably measure the LOSVD up to at least the fourth Gauss-Hermite moment h_4, we binned the PPAK spectra, using a Voronoi tesselation method (Cappellari & Copin 2003). We aimed for a minimal S/N of 50 for each bin. However, since the sky was not subtracted from our spectra, estimating a priori the S/N in the galaxy for each spectrum was not possible. We therefore prepared a second cube of PPAK spectra, extracted and reduced in exactly the same way as the original cube, except that we subtracted the sky based on the skyfibers that were positioned east and west of the main FoV, avoiding the skyfibers that fell directly in the galaxy. We binned the spectra based on the

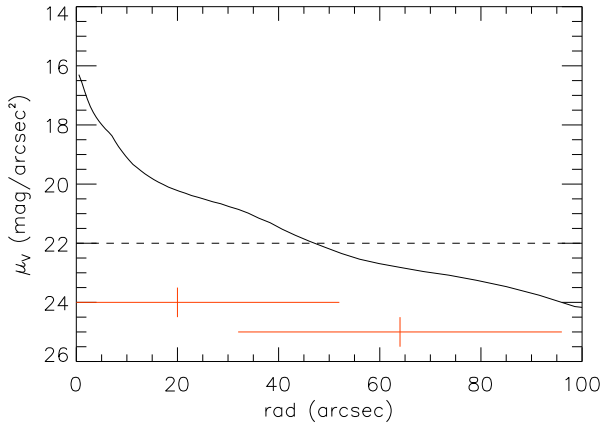

Figure 4.2 — Surface brightness in V-band as a function of radius in NGC 2549. The profile is obtained from MDM V-band imaging. The two solid horizontal lines indicate the extent of the PPAK FoV for our pointings (see also Figure 4.1), with the inner one centred at 1 R_e (fields B+C) and the outer one at 3.2 R_e (fields A+D). The dashed line indicates the surface brightness of the sky.

flux in this skysubtracted datacube, and continued our analysis with the original cube that still contained the sky. After extracting the kinematics, we checked that indeed the required minimal S/N was reached.

4.3.1 Stellar kinematics

We used the penalized Pixel Fitting[3] (pPXF) routine of Cappellari & Emsellem (2004) to extract the stellar kinematics from our spectra. pPXF convolves an optimal stellar template with the LOSVD, to find the best fit to the observed spectrum. During this fit, emission and sky lines are masked and therefore not included in the fit. The optimal stellar template is composed by pPXF for each bin as a linear combination of stellar spectra from a representative library. For this, we used the MILES library of 945 stars from Sánchez-Blázquez et al. (2006). We first co-added all the PPAK spectra of NGC 2549 together and then fitted this spectrum with pPXF, using the full MILES library to supply templates. The optimal template consisted of 51 MILES stars, and these stars were subsequently fed to pPXF as template library when fitting the binned spectra. We included additive polynomials to allow for changes in line strengths. Errors are obtained by a Monte Carlo simulation, by measuring the kinematics from many realisations of the input spectra, on which we added noise.

[3]available from http://www-astro.physics.ox.ac.uk/∼mxc/idl/#ppxf

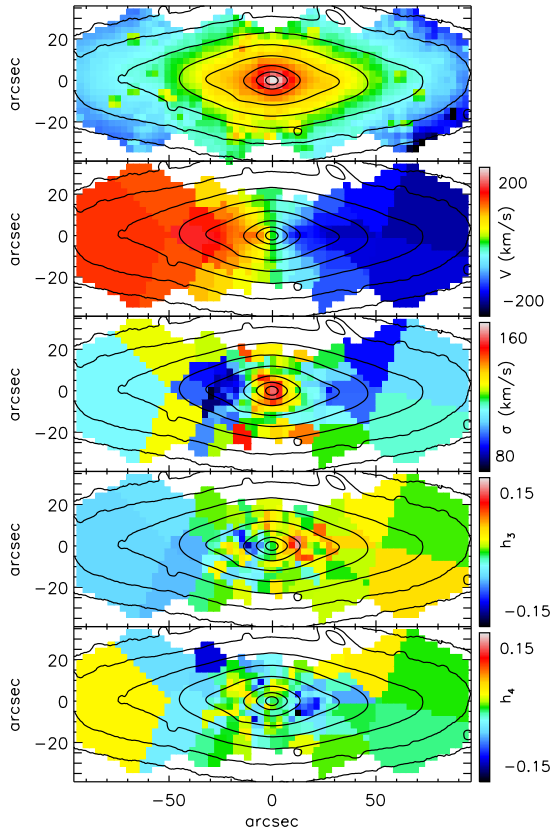

Figure 4.3 — Stellar kinematics extracted from the PPAK spectra of NGC 2549. From top to bottom: total flux, velocity, velocity dispersion, h_3 and h_4. The maps are orientated such that North is to the left and East is down. For a colour version of this plot, see the colour supplement.

By coadding the spectra of each blank sky exposure, we obtained sky spectra that we included as templates in pPXF. Since our spectra in the outer parts of the galaxy are very sky dominated, this way we obtain a more accurate sky subtraction, allowing for subtle sky variations. This procedure was introduced in Weijmans et al. (2009a) to fit sky dominated spectra, and we refer the reader to this paper for more details.

The LOSVD, parametrized by mean velocity V, velocity dispersion σ and the Gauss-Hermite moments h_3 and h_4 is shown in Figure 4.3. The spectra on the minor axis at the edge of the observed field had a somewhat deviant continuum shape around the Hβ absorption line, and we therefore removed these bins from the maps and forthcoming analysis. We fitted the LOSVD up to the 6th moment, but since h_5 and h_6 consisted mostly of noise, we did not include them in the subsequent analysis and modeling of the stellar kinematics, and therefore they are not shown here. NGC 2549 displays regular, disc-like rotation out to at least 4 R_e,

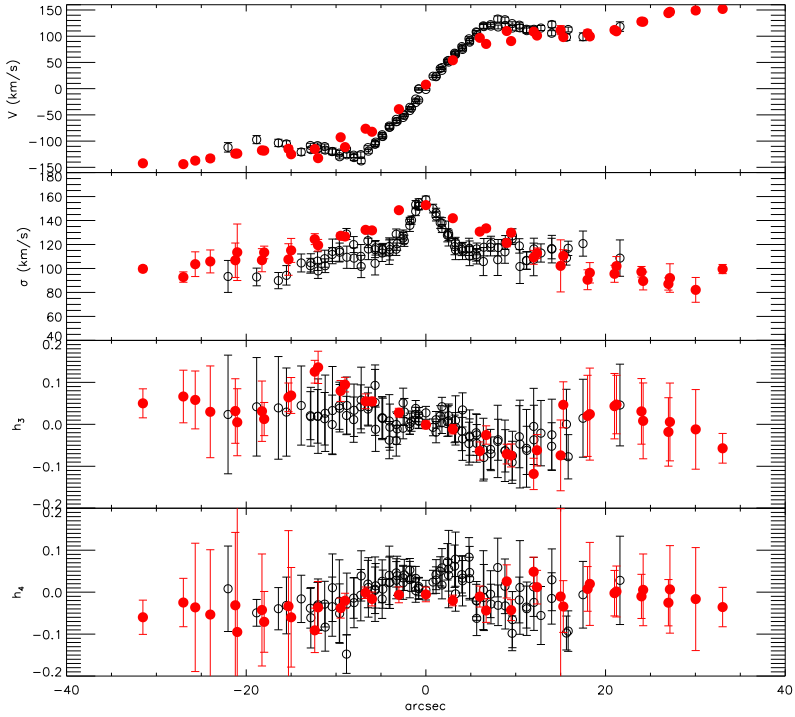

Figure 4.4 — Comparison between the PPAK (solid black dots) and SAURON (open grey circles) kinematics, along the major axis of NGC 2549. Observed errors in the PPAK data decrease at larger radii, as here more spectra are combined in single bins, to increase the total S/N.

while the velocity dispersion shows a drop of approximately 30 km s^{-1} around 20 arcsec accompagnied by a rise around 30 arcsec on the major axis, which could point to a cold disc embedded in a larger disc or bulge. Krajnović et al. (2008) also found two disc-like rotating components in this galaxy based on harmonic decomposition of its SAURON velocity map. They place the second component at 13 arcsec.

In Figure 4.4 we compare the stellar kinematics obtained with PPAK with the higher resolution SAURON kinematics in the central part of the galaxy. The SAURON kinematics of NGC 2549 were originally presented by Emsellem et al. (2004), but re-extracted with the MILES library (see Cappellari et al. 2007; Krajnović et al. 2009). Although the observed velocity, h_3 and h_4 agree between the two datasets, the PPAK data show a slightly higher velocity dispersion than the SAURON data. However, due to differences in sampling and spaxel size it is not straightforward to compare these values directly.

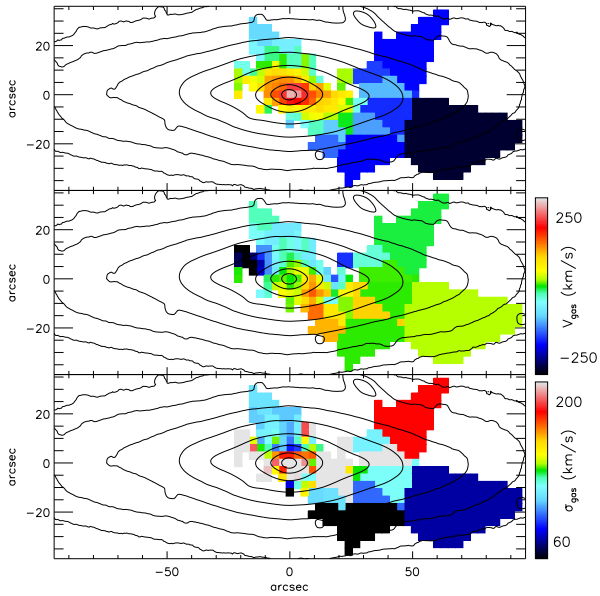

Figure 4.5 — Gas kinematics of NGC 2549, measured from [O III]. From top to bottom: flux, velocity and velocity dispersion. Only bins with amplitude-to-noise $A/N > 4$ are shown. Maps are orientated as in Figure 4.3. See the colour supplement for a colour version of this figure.

4.3.2 Ionised gas

There is some ionised gas present in NGC 2549, and emission line regions (He II, Hβ, [O III], [N I]) were masked during the extraction of the stellar kinematics. To determine the gas content and kinematics, we use the Gas AND Absorption Line Fitting[4] (GANDALF) routine described by Sarzi et al. (2006). GANDALF treats the emission lines as additional Gaussian templates and solves for their velocities and dispersion in combination with a stellar template convolved with the best fitting LOSVD found by pPXF. Multiplicative polynomials were included to fit the shape of the continuum. Since [O III] is the strongest emission line, we first fitted this doublet line, while keeping the other lines masked. We subsequently fitted all emission lines simultaneously, but kept their kinematics fixed to the [O III] kinematics. The skylines were masked during this procedure. We found no evidence for He II and [N I] emission, and only a few spurious detections of Hβ. [O III] was clearly detected in the inner part of the galaxy, and the [O III] gas maps are presented in Figure 4.5. The morphology and kinematics of the [O III] gas agree

[4]available from http://star-www.herts.ac.uk/∼sarzi/PaperV_nutshell

Index	Central bandpass (Å)	Blue continuum (Å)	Red continuum (Å)	Applied offsets (Å)
Fe4383	4369.125 - 4420.375	4359.125 - 4370.375	4442.875 - 4455.375	0.46 ± 0.05
Ca4455	4452.125 - 4474.625	4445.875 - 4454.625	4477.175 - 4492.125	0.36 ± 0.02
Fe4531	4514.125 - 4559.250	4504.250 - 4514.250	4560.500 - 4579.250	0.07 ± 0.03
$C_2$4668	4634.000 - 4720.250	4611.500 - 4630.250	4742.750 - 4756.500	-0.23 ± 0.05
Hβ	4847.875 - 4876.625	4827.875 - 4847.875	4876.625 - 4891.625	-0.09 ± 0.02
Fe5015	4977.750 - 5054.000	4946.500 - 4977.750	5054.000 - 5065.250	0.40 ± 0.04
Mg b	5160.125 - 5192.625	5142.625 - 5161.375	5191.375 - 5206.375	0.03 ± 0.02
Fe5270	5245.650 - 5285.650	5233.150 - 5248.150	5285.650 - 5318.150	0.07 ± 0.02
Fe5335	5312.125 - 5352.125	5304.625 - 5315.875	5353.375 - 5363.375	-0.04 ± 0.02
Fe5406	5387.500 - 5415.000	5376.250 - 5387.500	5415.000 - 5425.000	-0.07 ± 0.02
Fe5709	5696.625 - 5720.375	5672.875 - 5696.625	5722.875 - 5736.625	0.05 ± 0.01

Table 4.4 — Bandpass definitions of line strength indices (Trager et al. 1998), and offsets to the Lick/IDS spectrum from the MILES library.

with the SAURON results from Sarzi et al. (2006). The gas lies in a wide filament stretching from the Northwest to the Southeast in the galaxy, and is kinematically misaligned from the stellar rotation axis.

4.3.3 Line strength measurements

The relatively long wavelength coverage of PPAK (4300 - 5800 Å) allows us to measure a variety of absorption line strengths, such as Hβ, Mg b and various Fe indices. These indices are summarized in Table 4.4, with definitions taken from Trager et al. (1998). We adopt the procedure of Kuntschner et al. (2006) to measure the indices. We first removed the observed [O III] gas emission with an amplitude-to-noise ratio $A/N > 4$ from our spectra, and calibrated to the Lick/IDS system by broadening the spectra to the wavelength-dependent instrumental resolution of the Lick spectra (Worthey & Ottaviani 1997). The observed line strengths were corrected for broadening caused by the LOSVD.

Since the Lick spectra are not flux-calibrated, we need to apply offsets to our measured indices to conform to the Lick/IDS system. To determine these offsets, we had observed 11 different standard stars from the MILES library with PPAK during the same run. Each star was observed 2-3 times. In Figure 4.6, we show the line strength measurements of these stars, compared to the line strengths as measured directly on the spectra from the MILES library. Since both our PPAK spectra and the spectra from the MILES library are flux-calibrated, these offsets should be zero. We find that for most indices this is indeed the case, except for the most blue and most red indices. We therefore suspect that the flux-calibration on these parts of the spectra have not been perfect. We also see large deviations

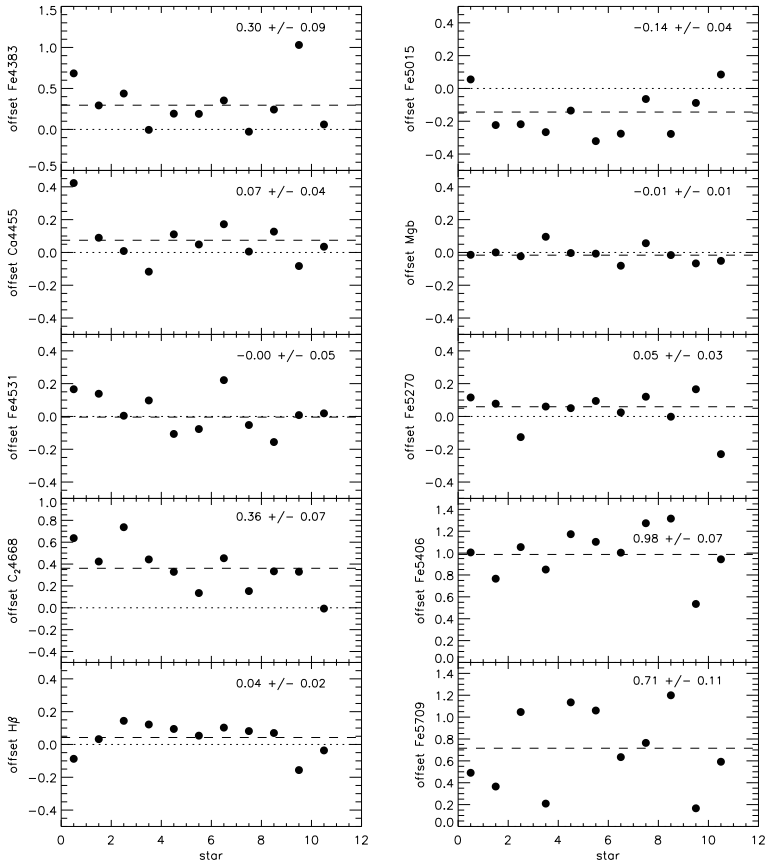

Figure 4.6 — Offsets in line strength indices as measured from our observed stars and as measured directly from the MILES library. The offsets are defined as MILES - PPAK, and are printed in the upper right corner of each panel. Errors are standard deviations divided by $\sqrt{N}$, with N the number of observed stars (which in this case means $N = 11$). Dashed lines correspond to the mean offset, dotted lines indicate an offset of zero. See text for more details.

for the Fe5335 index, but these are most likely caused by features resulting from a bad column on the CCD around this wavelength range.

Since for most indices our line strength measurements agree with those from the MILES library, we determined offsets to the Lick/IDS system using all the 235 stars in common between the Lick and MILES libraries. These offsets can be found in Table 4.4, and were applied to our data.

We present maps of the measured indices in Figure 4.7. Errors were determined with Monte Carlo simulations, where we took the noise of our observed

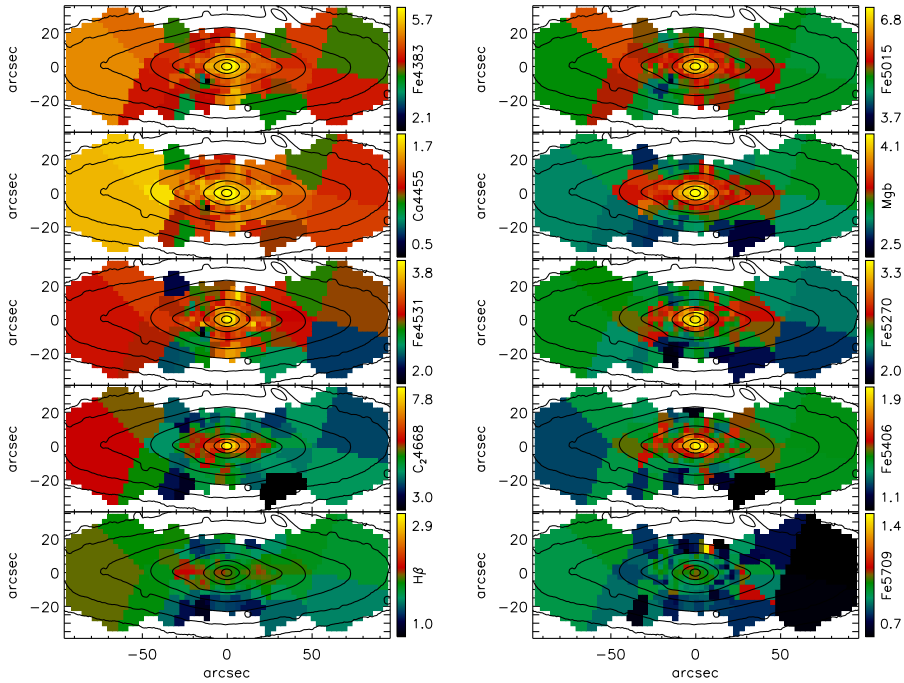

Figure 4.7 — Line strength maps of NGC 2549. Maps are orientated such that North is to the left and East down. The Fe5335 line strength map has been omitted, as this index was affected by a bad column on the CCD and could therefore not be reliably measured. See the colour supplement for a colour version of this figure.

spectrum and the uncertainty in radial velocity into account.

We compared our line strength measurements of NGC 2549 with those observed with SAURON and presented by Kuntschner et al. (2006) for those line strengths that we have in common (i.e. Hβ, Fe5015 and Mg b). For Hβ and Mg b these values agree within the errors introduced by applying different Lick offsets, but for Fe5015 the offset between the two datasets is larger, up to 0.9Å. This difference could be caused by a different removal of the [O III] lines from the spectra, as the measurement of this index critically depends on the treatment of this emission line. However, also in literature offsets between different datasets are mentioned (e.g. McDermid et al. 2006), and different values for offsets from flux-calibrated spectra to the Lick system are reported for different instruments (e.g. Kuntschner 2000; Norris, Sharples & Kuntschner 2006; Sánchez-Blázquez et al. 2009).

4.4 Stellar population models

We now turn our attention to the properties of the stellar population in NGC 2549. For our analysis we use the Hβ, Fe5015, Mg b and Fe5270 indices, as these indices can be well measured and show the most stable maps and offsets (see Figures 4.6 and 4.7). In order to avoid dependence on α-enhancement [α/Fe], we couple the iron and Mg b indices into the following abundance ratio insensitive indices (Kuntschner et al. in prep):

$$[\mathrm{MgFe50}]' = \frac{0.69 \times \mathrm{Mg}b + \mathrm{Fe5015}}{2}, \tag{4.1}$$

$$[\mathrm{MgFe52}]' = \frac{0.64 \times \mathrm{Mg}b + \mathrm{Fe5270}}{2}. \tag{4.2}$$

Our main goal in this section is to estimate the stellar mass-to-light ratio M_*/L, as this value is currently one of the main uncertainties when constructing mass models including dark matter. For the first time we are now able to use IFU data to generate M_*/L maps, based on line strength measurements.

4.4.1 Single stellar population modeling

We employ the stellar population models based on the MILES library (Sánchez-Blázquez et al. 2006; Vazdekis et al. in prep.) for our analysis. These models predict line strength indices, colours and stellar mass-to-light ratios (M_*/L) for different combinations of age, metallicity and initial mass function (IMF). We fix the IMF to the Kroupa IMF (Kroupa 2001) and find the predicted line strength indices and M_*/L for a grid uniformly sampled in metallicity and log(age). Since the original models are sparsely sampled in metallicity ([Z/H]= -0.71, -0.40, 0.00 and 0.22) and not uniformly sampled in log(age), we interpolated the tables generated by the models to construct this uniform grid. Next, we used a maximum likelihood estimator to find the most likely value for M_*/L, given the observed line strength indices. Errors were determined by 68 per cent confidence intervals in the probability distributions.

We repeated the above analysis for each bin in our PPAK data cube, and thus were able to generate maps of M_*/L, as well as age and metallicity. These maps are shown in Figure 4.8. We find that both the stellar M/L and age are reasonably constant over the total FoV, out to 4 R_e. For M_*/L in R-band we find a value of 2.6 $\pm$ 0.6 $M_\odot/L_{\odot,R}$, while the age of the stellar population is about 9 $\pm$ 5 Gyr,

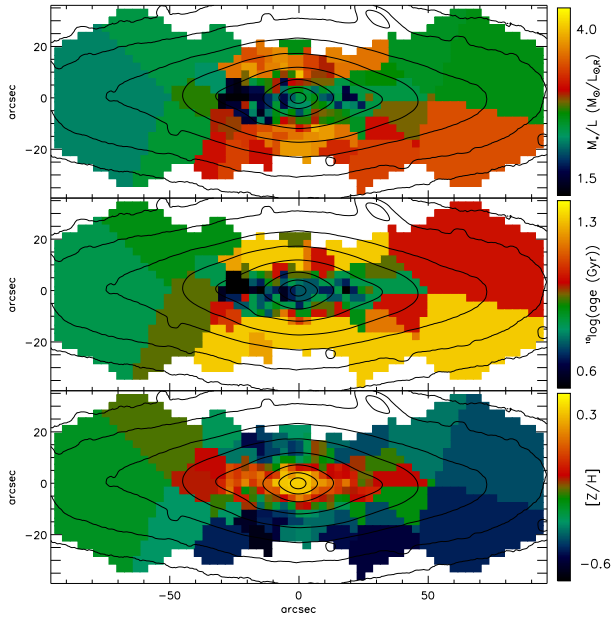

Figure 4.8 — From top to bottom: stellar mass-to-light ratio (M_*/L) in R-band, age and metallicity ([Z/H]) in NGC 2549. Maps are again orientated with North to the left and East down. See the colour supplement for a colour version of this figure.

though younger in the central part of the galaxy. The metallicity is enhanced in the centre, and it drops from [Z/H] = 0.2 in the centre to -0.4 at large radii.

It would be interesting to see how our maps of M_*/L, age and metallicity compare to maps obtained using colours instead of line indices (see Zibetti, Charlot & Rix 2009 for a demonstration of this method). Since this would require very accurate colours out to large radii and a well-understood calibration between different photometry bands, as well as a correction for galactic extinction, we do not make this comparison here. For future projects it will be fruitful to obtain deep imaging in different optical and near-infrared bands, in addition to deep integral-field spectrography.

4.4.2 Two components in NGC 2549?

In the stellar kinematic maps we see hints for a cold disc, embedded in a thicker disc or bulge. To look for evidence for an embedded disc in the line strengths, we start by plotting the indices as a function of radius, to determine the line strength gradients. The slopes of these gradients provide clues on the formation scenario

of the galaxy, with steep gradients resulting from monolithic collapse (Carlberg 1984), while mergers dilute existent gradients (White 1980). More recent simulations however have shown that depending on the gradients in the parent galaxies, the merger remnant can have either a steeper or a shallower gradient than its progenitors (Di Matteo et al. 2009) and that a combination of monolithic collapse and hierarchical galaxy formation is required to reproduce the gradients that are observed in early-type galaxies (Kobayashi 2004).

Before plotting the gradients, we first transform our observed indices into magnitudes:

$$\text{index}' = -2.5\log(1 - \frac{\text{index}}{\Delta\lambda}), \tag{4.3}$$

where $\Delta\lambda$ is the width of the central bandpass (see Table 4.4), and the index in magnitudes is denoted by a prime [$'$]. Next, we average the indices along the isophotes of the galaxy, taking the flattening of the galaxy into account. We plot our results in Figure 4.9. We find no change in the line strength gradients, in fact: the slopes remain constant from 0.1 R_e out to at least 4 R_e. Hopkins et al. (2009b) sketch a scenario in which a secondary starburst following a major merger steepens the line strength gradients in the inner part of the galaxy, while violent relaxation flattens these gradients at larger radii. We find no support for this scenario, which would be an indication of a second component, although it remains possible that the merger happened sufficiently long ago (more than several Gyr) and that therefore the expected change in line strength slope between the young disc and older bulge has dissappeared. We note that the slope of the metallicity gradient seems to flatten in the inner 5 arcseconds of the galaxy, however data with higher spatial resolution is needed to investigate this further.

Norris et al. (2006) used line strength profiles along the major and minor axis to identify a young disc embedded in an old bulge in the lenticular galaxy NGC 3115. Since the disc in this galaxy is more flattened than the bulge, they found a difference in gradient between the major and minor axis. To investigate whether NGC 2549 shows similar behaviour, we select the bins that are located within 3 arcsec from the major and minor axis, and plot their radial profiles (see Figure 4.9). We correct the distance along the minor axis by taking the flattening into account. We find no distinction in line strength behaviour between the major and minor axis on the galaxy. In the metallicity profile however we see a small difference in slope between the minor and major axis, which could indicate that indeed a thin metal-rich disc is present, embedded in a thicker, metal-poorer disc. This view is strengthened by the metallicity map (Figure 4.8), where the

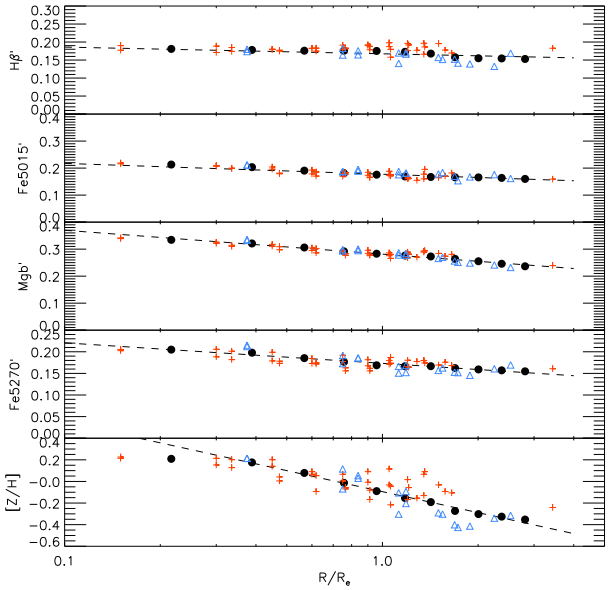

Figure 4.9 — Line strength indices (from top to bottom Hβ, Fe5015, Mg b and Fe5270) in magnitudes, and metallicity [Z/H], as a function of radius. Black dots denote averaged line strengths along the isophotes of the galaxy, while the crosses and open triangles denote measurements along the major and minor axis, respectively. The minor axis radii have been corrected for the flattening of the galaxy. Errorbars are comparable to the size of the plotting symbols.

iso-metallicity contours appear more flattened than the isophotes. This effect has been observed in several other fast-rotators (e.g. Kuntschner et al. in prep.).

4.5 Dynamical models

In this section we investigate whether a dark matter halo is needed to fit the observed stellar kinematics of NGC 2549, and constrain the amount of dark matter. We use the triaxial Schwarzschild modeling code of van den Bosch et al. (2008), which was extended to allow for the inclusion of a dark matter halo by Weijmans et al. (2009a). Briefly, a mass distribution is constructed by combining a dark halo, black hole and a deprojection of the observed stellar surface brightness. Orbits are then calculated in the potential constructed from the mass distribution. These orbits are then combined into a superposition, that best fits the observed kinematics, while constraining the fit such that it reproduces the stellar mass distribution.

4.5.1 Schwarzschild models

NGC 2549 is an edge-on fast rotator (c.q. discy elliptical) that shows no signs of a strong bar and can therefore be reasonably modeled with an oblate axisymmetric mass distribution. Krajnović et al. (2009) presented axisymmetric Schwarzschild models of NGC 549 and we use their best-fitting model as a starting point. We adopt their inclination of 88°, and (a close to) oblate geometry. We fix the black hole mass to their best-fit value $M_\bullet = 1.4 \times 10^7\ M_\odot$. We adopt their dynamical $M/L = 4.7\ M_\odot/L_{\odot,R}$ for the stellar M/L (constructing a maximal spheroid model), as well as their Multi-Gaussian Expansion (MGE, see Emsellem, Monnet & Bacon 1994; Cappellari 2002) mass model. This MGE model is based on HST/WFPC 2 imaging in R-band, complemented with wide-field MDM imaging in V-band, that was scaled to match the WFPC 2 image. We added a spherical halo with a NFW profile to the total potential :

$$\Psi_{\rm halo}(r) = -4\pi G\rho_s r_s^2 \frac{r_s}{r} \ln(1+\frac{r}{r_s}), \tag{4.4}$$

with G the gravitational constant, ρ_s a characteristic density and r_s a characteristic radius. These last two quantities are coupled to the concentration parameter c of the halo and the halo mass M_{200}, which is the total mass of the halo within r_{200}:

$$\frac{\rho_s}{\rho_{\rm crit}} = \frac{200}{3} \frac{c^3}{\ln(1+c) - c/(1+c)}, \tag{4.5}$$

$$M_{200} = 4\pi\rho_s r_s^3 [\ln(1+c) - \frac{c}{1+c}]. \tag{4.6}$$

Here r_{200} is the radius within which the mean density of the halo has dropped to 200 times the critical density $\rho_{\rm crit}$.

For now, we fix the concentration of the halo to $c = 10$, to be consistent with predictions from cosmological simulations (Bullock et al. 2001) and to reduce the parameter space that needs to be searched. We then optimized the models by varying the halo mass M_{200}, while fitting the PPAK kinematics up to the fourth Gauss-Hermite moment h_4, as well as the SAURON kinematics (Emsellem et al 2004; Krajnovic et al. 2009) up to h_6, which cover the central R_e of the galaxy with higher spatial resolution.

The PPAK data shows a somewhat higher velocity dispersion than the SAURON data (see Figure 4.4). Since we combine the two datasets here in one dynamical

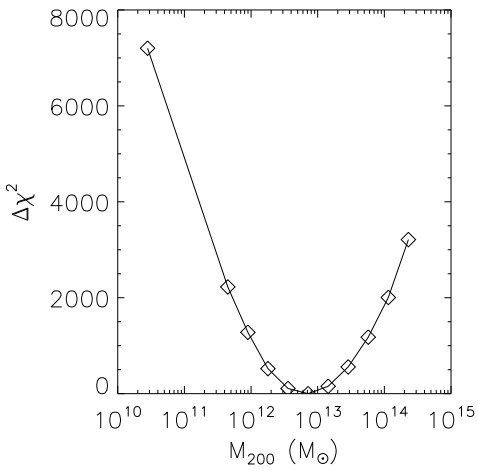

Figure 4.10 — $\Delta\chi^2$ levels for the Schwarzschild models of NGC 2549. The only free parameter in these models is M_{200} (total halo mass). The model without dark halo is relocated at 3×10^{10}, to place it within the plot.

model, a pragmatic solution is to scale the PPAK velocity dispersions to agree with the SAURON ones. After some experimentation we found that a quadratic correction worked best:

$$\sigma_{\rm model} = \sqrt{\sigma^2_{\rm PPAK} + \sigma^2_{\rm instr} - \sigma^2_{\rm corr}}, \tag{4.7}$$

with $\sigma_{\rm instr}$ the instrumental resolution (103 km s^{-1}) and $\sigma_{\rm corr}$ a correction term. We found a correction of 110.5 km s^{-1} to minimize the differences between the SAURON and the PPAK observations, while taking the different seeing into account. We then applied this correction term to the PPAK dispersion.

In Figure 4.10 we show the χ^2 for the different halo masses. The amount of dark matter is constrained well, due to the flat rotation curve and the rising dispersion at large radii. The halo has a mass of $M_{200} = 7 \times 10^{12}\ M_\odot$. The kinematics of the best-fitting model are shown in Figure 4.11. The model reproduces the mean stellar velocity very well. The dispersion out to 30 arcsecond is also reproduced nicely, but the dispersion rise at larger radii along the major axis can not be reproduced by the spherical NFW halo. Therefore the models also fail to reproduce the higher moments, as they have relatively larger errors. Hopefully, dark haloes with a large central core and a lower stellar M/L will be able to reproduce the data. Given the large spatial extent of the PPAK data we should be able to constrain the mass distribution of the halo, and this is currently under investigation.

In Figure 4.12 we show the anisotropy of our best-fitting model, compared

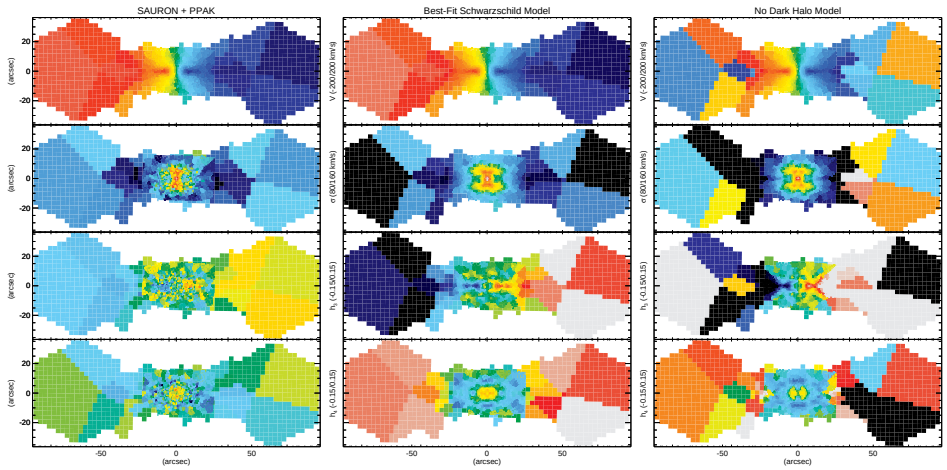

Figure 4.11 — Point-symmetrized kinematics of the SAURON and PPAK data and the best-fitting model with a spherical NFW halo. The model reproduces the flat rotation curve well, but has trouble reproducing the rising dispersion at radii larger than 40 arcseconds. Consequently, the higher moment at those radii cannot be reproduced either. The model without a dark halo cannot reproduce the observed rotation field, and is overall a poor fit to the data. A larger colour version of this figure can be found in the colour supplement.

to a model without halo and a model with a too heavy halo. We parametrize the anisotropy with

$$\beta_r = 1 - \frac{\sigma_\phi^2 + \sigma_\theta^2}{2\sigma_r^2}, \tag{4.8}$$

where (r, θ, ϕ) are the standard spherical coordinates. For all models β_r is low, which means that the stellar orbits are strongly tangentially anisotropic. This is a clear signature of a disc-like structure. In contrast to what is seen in spherical or axisymmetric models (e.g. Richstone & Tremaine 1984; Dekel et al. 2005), we do not see an increase of radial anisotropy with increasing halo mass. This behaviour should be investigated in more detail. However, the higher moments are currently not well produced in the model and they typically constrain the amount of anisotropy.

After inspecting the distribution of the orbits in the Schwarzschild model we found that the system is made up out of three distinct components: a compact bulge, a small (inner) thin disc and a large thick disc, similar to what was found by Krajnović et al. (2008). As the this disc is (perhaps) also seen in the metallicity map, it would be interesting to look into these separate phase space components

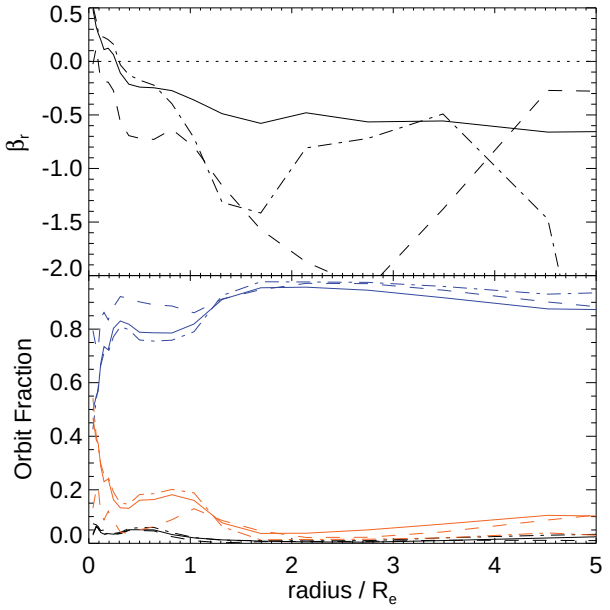

Figure 4.12 — Orbital structure of NGC 2549. Top panel: velocity anisotropy β_r as a function of radius (see Equation 4.8). The solid line indicates our best-fitting model ($M_{200} = 7 \times 10^{12}\ M_\odot$), the dashed and dashed-dotted line denote the model without halo and the model with a too heavy halo ($M_{200} = 3 \times 10^{13}\ M_\odot$), respectively. Bottom panel: fraction of orbit types as function of radius for the models of the top panel. Blue lines denote fractions of short axis tubes, red lines long axis tubes and black lines the fractions of box orbits. See the colour supplement for a colour version of this figure.

in more detail, at it might allow us to measure the metallicities of the three components individually.

4.5.2 Jeans anisotropic models

In addition to Schwarschild models, we also constructed Jeans anisotropic models of our dataset. These axisymmetric models are based on the second velocity moments, given by:

$$V_{\rm rms} = \sqrt{V^2 + \sigma^2}, \tag{4.9}$$

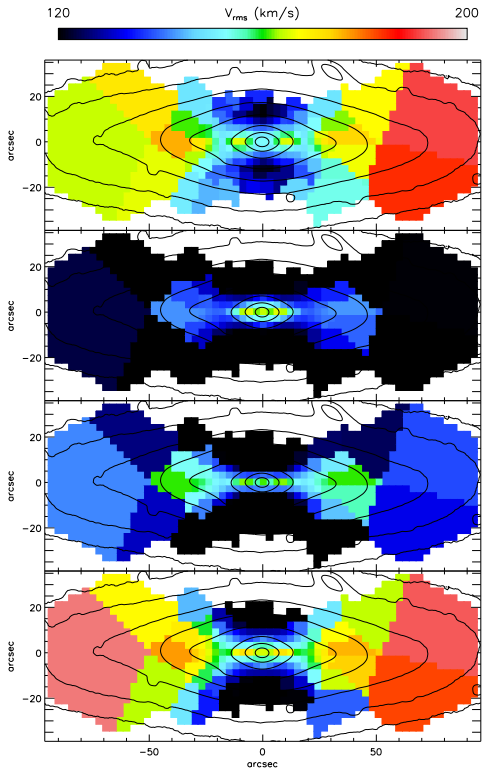

Figure 4.13 — Jeans anisotropic models of NGC 2549, based on the second velocity moments of the PPAK kinematics. From top to bottom: bi-symmetrized observations, model without dark halo and β_z = 0.17, model without dark halo withβ_z = 0.17 for $R < 20$ arcsec and β_z = -10 for $R > 20$ arcsec, and the finally the best-fitting model with an NFW halo and β_z = 0.17. See the colour supplement for a colour version of this figure.

and are characterized by the anisotropy parameter β_z, which is defined as:

$$\beta_z = 1 - \overline{v_z^2}/\overline{v_R^2}. \tag{4.10}$$

This modeling method is explained in detail by Cappellari (2008), who also presented a mass model of NGC 2549 based on the SAURON observations. His best-fitting model is edge-on (i = 90°) and has β_z = 0.17. Adopting these values we try to construct a Jeans model to reconstruct the observed PPAK kinematics, but we find that we cannot construct a mass model without extra dark matter, even if we allow for an extreme anisotropy in the outer parts of the galaxy (see Figure 4.13). We therefore add a spherical NFW halo to the model, with $c = 10$ to be consistent with the Schwarzschild models. The dark halo is included in the fit as a one-dimensional MGE model and we fit for M_{200} and M_*/L. We find a

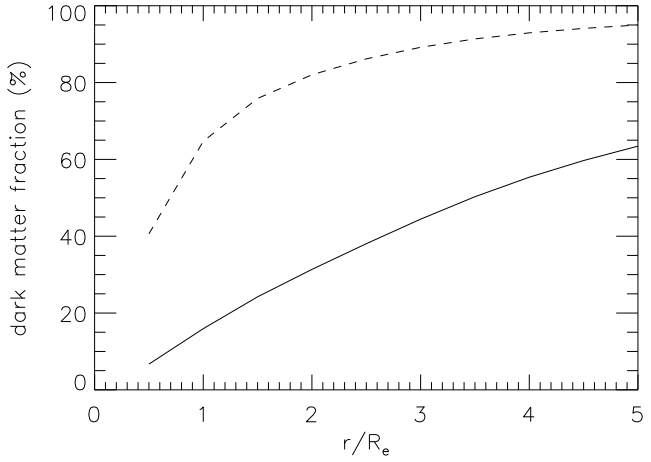

Figure 4.14 — Enclosed dark matter fraction as a function of radius. The solid line denotes the best-fitting maximum spheroid model with $M_*/L = 4.7 M_\odot/L_{\odot,R}$, while the dashed line follows the model with $M_*/L = 2.6 M_\odot/L_{\odot,R}$, consistent with stellar population models.

good fit to the data (see Figure 4.13), with a best-fitting halo mass of M_{200} = 1.3 $\times$ 10^{13} $M_\odot$, which is within a factor of two with the best-fitting halo mass found by the Schwarzschild model. This agreement is very encouraging and provides confidence for our results, as these two modeling methods work from different principles. The Jeans models can also reproduce the increase of $V_{\rm rms}$ at larger radii. This quantity is mostly dominated by the rotation of the system, which is large compared to the velocity dispersion.

The best-fitting stellar M/L is 5.5 $M_\odot/L_{\odot,R}$ which deviates from the value found by Schwarzschild modeling. However, the Jeans models were fitted to the PPAK data only, which were not corrected for the offset between the PPAK and SAURON velocity dispersions. Scott et al. (2009) present anisotropic models of NGC 2549 based on SAURON kinematics and find a best-fitting M/L of 4.8 $M_\odot/L_{\odot,R}$, in agreement the Schwarzschild models of Krajnović et al. (2009).

4.5.3 Dark matter fractions

In Figure 4.14 we show the enclosed dark matter fraction as a function of radius for our best-fitting Schwarzschild model. The total stellar mass in this model is 2.8 $\times$ 10^{10} $M_\odot$, which is a factor $\sim$ 250 smaller than the total halo mass M_{200} = 7 $\times$ 10^{12} $M_\odot$. Within 1 R_e, 16 per cent of the total mass is dark, while within 5 R_e, this percentage has grown to 63 per cent. Note however that this model assumes

a maximal spheroid, and that therefore these percentages are lower limits.

Since we also have an estimate of the stellar M/L based on stellar population modeling, we scaled our Schwarzschild models to this value. This resulted in a decrease of almost 50 per cent in stellar mass, as now M_*/L was fixed to 2.6 $M_\odot/L_{\odot,R}$, instead of the maximal allowed value of 4.7 $M_\odot/L_{\odot,R}$. Consequently, the mass of the best-fitting dark halo increased, to compensate for the loss in stellar mass. The best-fitting halo for this model has $M_{200} = 1 \times 10^{15}\ M_\odot$, again assuming an NFW profile with a concentration $c = 10$. The dark mass inside 1 R_e for this model corresponds to 65 per cent of the total mass, increasing to 95 per cent at 5 R_e (see also Figure 4.14). However, this model overpredicts the velocity dispersion at larger radii, and therefore M_*/L is most likely underestimated. This implies however that the dark matter fractions in NGC 2549 are bracketed by the values quoted here for these two extreme models.

The difference in M_*/L as determined by the maximal spheroid model and the stellar population models seems rather large, but a comparable difference between these two values was observed by Weijmans et al. (2008) for the early-type galaxy NGC 2974. They determined dark matter fractions in this galaxy, using the kinematics of a large H I ring surrounding this system. For the two early-type galaxies NGC 3379 and NGC 821, studied by Weijmans et al. (2009a), the difference between dynamical and stellar M/L was much smaller (see also Cappellari et al. 2006), and these systems seem to be less dark matter dominated than NGC 2549. It is interesting to note that both NGC 2549 and NGC 2974 are disc-like galaxies that show rotation out to at least 5 R_e, while NGC 3379 and NGC 821 are both rounder and show little rotation at large radii. However, a comparison between the different models for these galaxies is not straightforward because of the maximal spheroid assumption. A more thorough analysis is needed to make a fair comparion between these models, but this is currently beyond the scope of this text.

4.6 Discussion and summary

We observed the early-type galaxy NGC 2549 with the integral-field spectograph PPAK out to at least 4 R_e. We obtained integrations of several hours and in the outer part of the galaxy binned individual spectra together, to obtain sufficient signal-to-noise to measure both stellar kinematics and absorption line strengths. The velocity map displays regular rotation out to the edge of the observed field, while the velocity dispersion has a declining profile, followed by a slight increase outside 30 arcsec. Using stellar population models and the observed line strengths

as constraints, we constructed maps of age, metallicity and stellar M/L. The metallicity map shows evidence for a younger, metal-rich disc-like component, embedded in a larger disc or bulge. Further hints for an embedded disc were presented by Krajnović et al. (2009), who reported the presence of two disc-like components based on the SAURON stellar kinematics. Our Schwarzschild model, based on the new PPAK spectra, complemented with SAURON kinematics for the central part of the galaxy, also show evidence for embedded components: we identify from the orbital structure a compact bulge, a thin inner disc and a large thick disc. These observations provide hints for the merger and starformation history of NGC 2549. One would expect to find an inner disc as we described here, as a result from secondary starformation after a major merger (e.g. Hopkins et al. 2009b).

From our Schwarzschild model we find that a dark halo is required to reconstruct the observed kinematics. We explored possible halo masses of a spherical NFW halo, with a concentration $c = 10$, whithin the maximum spheroid (or minimal halo) assumption. The best-fitting halo mass agrees with the one obtained from anisotropic Jeans modeling of the PPAK kinematics. Since the two modeling methods arise from different principles, the agreement in halo mass is very encouraging. We find that within 1 R_e at least 16 per cent of the total mass is dark, while within 5 R_e this percentage has grown to 63 per cent. However, if we adopt the stellar M/L found by stellar population modeling, NGC 2549 becomes much more dark matter dominated: already within 1 R_e more than half (65 per cent) of the total mass lies within the dark halo. However, even within the same stellar population model, differences in initial-mass function, treatment of stellar winds and lower-mass cuts can introduce large uncertainties (up to 40 per cent) in M_*/L.

Our Schwarzschild model cannot exactly reproduce the observed behaviour of the velocity dispersion at larger radii. This could be caused by the restrictions that we have emposed on our halo model. To limit the parameter phase, we only explored spherical haloes with a (cuspy) NFW profile. However, simulations have shown that haloes are most likely flattened or triaxial (e.g. Hayashi, Navarro & Springel 2007), while observations of low-surface brightness and dwarf galaxies have found evidence for cored halo profiles (e.g. Weldrake, de Blok & Walter 2003; de Blok et al. 2008) Now that we have obtained stellar kinematics over the complete galaxy field out to 4 R_e instead of only major axis measurements (Weijmans et al. 2009a), we should start to explore whether we can constrain the shape and profile of the dark halo. If indeed it becomes possible to model the dark halo in such detail, this will provide important tests for galaxy formation theories.

Acknowledgements

It is a pleasure to thank Felix Hormuth and Sebastian Sánchez for preparing and performing our observations at Calar Alto. We also gratefully acknowledge Eric Emsellem, Davor Krajnović and Richard McDermid for fruitful discussions.

This research was supported by the Netherlands Organization of Scientific Research (NWO) through grants 614.000.426 and 614.000.301. MC acknowledges support from an STFC Advanced Fellowship (PP/D005574/1).

This work is based on observations collected at the Centro Astronómico Hispano Alemán (CAHA) at Calar Alto, operated jointly by the Max-Planck Institut für Astronomie and the Instituto de Astrofísica de Andalucía (CSIC).